LAWRENCE
LIVERMORE
NATIONAL
LABORATORY

LLNL-PROC-660409

Developing physics basis for the radiative snowflake divertor at DIII-D.

V. A. Soukhanovskii, S. L. Allen, M. E. Fenstermacher, C. J. Lasnier, M. A. Makowski, A. G. McLean, W. H. Meyer, D. D. Ryutov, E. Kolemen, R. J. Groebner, A. W. Hyatt, A. W. Leonard, T. H. Osborne, T. W. Petrie

September 16, 2014

IAEA 25th Fusion Energy Conference
St. Petersburg, Russia
October 13, 2014 through October 18, 2014

Disclaimer

Developing Physics Basis for the Radiative Snowflake Divertor at DIII-D.

V.A. Soukhanovskii[1], S.L. Allen[1], M.E. Fenstermacher[1], C.J. Lasnier[1], M.A. Makowski[1], A.G. McLean[1], W.H. Meyer[1], D.D. Ryutov[1], E. Kolemen[2], R.J. Groebner[3], A.W. Hyatt[3], A.W. Leonard[3], T.H. Osborne[3] and T.W. Petrie[3]

[1]Lawrence Livermore National Laboratory, 7000 East Ave, Livermore, CA 94550, USA
[2]Princeton Plasma Physics Laboratory, PO Box 451, Princeton, NJ 08543-0451, USA
[3]General Atomics, PO Box 85608, San Diego, CA 92186-5608, USA

Corresponding Author: vlad@llnl.gov

Abstract:
Recent DIII-D results demonstrate that the snowflake (SF) divertor geometry (cf. standard divertor) enables significant manipulation of divertor heat transport for heat spreading and reduction in attached and radiative divertor regimes, between and during edge localized modes (ELMs), while maintaining good H-mode confinement. Increased integral scrape-off layer (SOL) width and heat flux spreading over additional strike points (SPs) were observed in DIII-D, suggesting enhanced heat transport through the low poloidal field null-point region and divertor legs. Direct measurements of divertor null-region poloidal β_p, using a unique DIII-D divertor Thomson scattering diagnostic, were consistent with the theoretically proposed mechanism of instability-driven fast convective plasma mixing in the high-β_p region, especially efficient during ELMs. The peeling-ballooning mode stability in the H-mode discharges was not significantly affected in the SF configuration as the ELM frequency and size were changed by 10-20 %. The stored energy lost per ELM (i.e., ELM size) was reduced. In deuterium-seeded radiative regimes in 4-5 MW NBI-heated H-mode discharges, the SF geometry led to a significant reduction of peak heat fluxes between and during ELMs. The results complement the initial SF divertor studies in the NSTX and DIII-D tokamaks and contribute to the physics basis of the radiative SF divertor as a power exhaust concept for future tokamaks.

1 Introduction

Based on three decades of magnetically confined nuclear fusion plasma physics research, an axisymmetric magnetic X-point divertor is envisioned as the plasma-material interface for the tokamak-based reactor. Intense heat and particle fluxes from the core plasma are directed to a separate divertor chamber for mitigation and control. The steady-state mitigation techniques include partitioning the power that flows into the scrape-off layer (SOL) P_{SOL} between divertor targets, reducing parallel heat and particle fluxes via volumetric losses and radial spreading, and reducing the heat flux deposited on the plasma facing components (PFCs) via increasing the plasma-wetted area A_w [1, 2]. However, for future tokamaks, e.g., the fusion nuclear science facilities (FNSF) [3, 4] and DEMO [5], these techniques may be insufficient to control steady-state heat fluxes within the present

technological limit of 5-10 MW/m^2. Additionally, transient divertor heat fluxes from edge localized modes (ELMs) must be mitigated via ELM size reduction and peak heat flux reduction to the transient limit of 0.1-0.5 MJ/m^2.

A snowflake (SF) divertor magnetic configuration [6] has been proposed as a potential solution for the tokamak divertor power exhaust problem. Experiments performed in the TCV [7, 8, 9], NSTX [10, 11, 12] and DIII-D tokamaks [13] have provided encouraging results to support the physics basis for further SF divertor concept development for future high-power facilities. In particular, initial experiments in DIII-D and NSTX at high divertor power densities demonstrated significantly reduced inter-ELM and ELM divertor heat flux and compatibility with high performance operation (H98y2$\geq$1). In this paper we discuss recent DIII-D experiments that show that the SF divertor enables significant heat transport manipulation and heat flux spreading at attached and radiative divertor conditions between and during ELMs, w.r.t. the standard divertor. It is envisioned that the advanced divertor optimized for heat and particle flux mitigation would take advantage of a combination of techniques, e.g., the magnetic geometry, plasma-facing component (PFC) geometry and structure, and impurity-seeded radiative solutions.

2 Experiment

The SF divertor magnetic configuration uses a second-order null created by merging two first-order nulls of the standard divertor [6, 14]. Poloidal magnetic flux surfaces in the region of the exact second-order null form six separatrix branches with an appearance of a snowflake. The exact second-order null configuration is topologically unstable [6]: small variations of coil currents may lead to the break-up of the second order null into two physically separated first-order nulls. The two variants of the exact configuration often realized in steady-state experiments are called snowflake-plus and snowflake-minus. In the SF-plus, the secondary null is on the private flux region side of the standard divertor X-point. In the SF-minus, the secondary null is in the common flux SOL. Poloidal field B_p in the SF null region is a quadratic function of distance (vs linear in the standard divertor) [6], making the region of low B_p surrounding the null(s) broader (Fig. 1).

The SF divertor experiments were conducted in DIII-D using a standard highly-shaped lower single null H-mode discharge scenario with $B_t = 2$ T, $I_p = 1.2$ MA, $P_{NBI} \leq 5$ MW, and ion $B \times \nabla B$ drift toward the lower divertor. The DIII-D tokamak divertor is an open geometry divertor with graphite PFCs. A divertor cryo-pump was used for particle removal, and D_2 seeding was used for steady-state density control in the range $(0.4 - 0.7) \times n_e/n_G$ ($\sim 4.5 - 7.5 \times 10^{19}$ m^{-3} where n_G is the Greenwald density [15]).

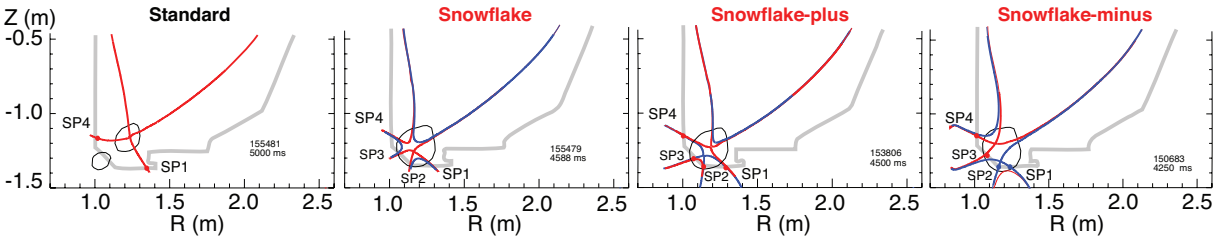

FIG. 1: Experimental equilibria of the standard, SF, SF-plus, and SF-minus divertor configurations. The primary separatrices are shown by the red lines, the secondary by the blue lines. The region $B_p \leq 0.1\ B_{pm}$, where B_{pm} is the outer midplane B_p, is shown by the line surrounding the null(s) region.

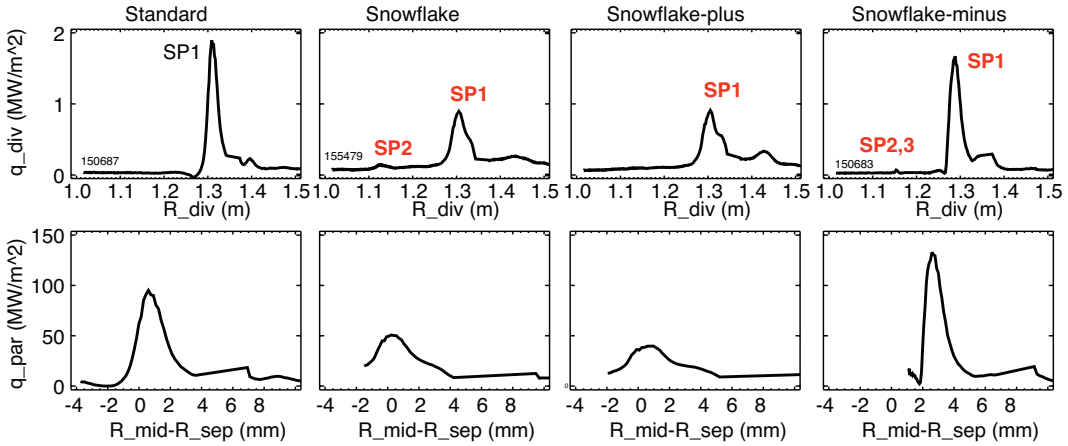

FIG. 2: Inter-ELM divertor deposited and parallel heat flux profiles in the standard ($D \simeq 20$ cm), SF ($D \leq 3$ cm), SF-plus ($D \leq 10$ cm), and SF-minus ($D \leq 11$ cm) configurations.

The SF configurations were obtained using three poloidal field shaping coils in the divertor region. The SF-minus configuration used a combination of pre-programmed coil currents and strike point position control by the plasma control system (as in Ref. [11]), while the exact SF and SF-plus were controlled using a real-time null-tracking algorithm [16]. The SF configurations were produced for long periods (2-3 s) exceeding energy confinement time $\tau_E \leq 0.250$ s and comparable with discharge flat-top duration of $3 - 4$ s. Magnetic equilibria were reconstructed with the standard Grad-Shafranov code EFIT.

3 Results

Recent DIII-D experiments focused on relative roles of geometry and transport in the SF divertor effects previously observed in DIII-D and NSTX, including: power sharing between additional strike points, divertor heat flux spreading, detachment onset and stability, as well as impact on pedestal stability and ELMs.

Geometric properties (e.g., the poloidal magnetic flux expansion f_{exp}, midplane-to-target connection length $L_{\|}$, and specific divertor volume V_{div}) of the SF-plus and the SF-minus are similar to those of the exact SF configuration when the distance D between the poloidal nulls satisfies $D \leq a\ (\lambda_q/a)^{1/3}$, where a is the minor radius and λ_q is the SOL power width as projected to midplane [14]. The increased $L_{||}$, V_{div} (proportional to $L_{||}$), and plasma-wetted area $A_{wet} = 2\pi R_{SP} f_{exp} \lambda_q$ (where R_{SP} is the strike point major radius) would lead to reduced divertor q_{peak} and increased divertor volumetric losses. The criterion yields $D \sim 10$ cm for DIII-D discharge parameters ($a \simeq 0.60$ m, $\lambda_q \simeq 2.5 - 3$ mm [17]). Distances $D = 0 - 12$ cm were typically realized in the experiment, leading to the expectation that the SF-plus and the SF-minus would behave much like the exact SF. If the distance D is remapped via ψ_N to the midplane, as is done with the dr_{sep} parameter in double-null magnetic configurations, one obtains $d_{XX} \leq 0 - 3$ mm (cf. SOL width λ_q).

Inter-ELM peak heat flux reduction in the SF divertor (cf. standard divertor) were observed in the experiments and attributed mostly to the increased A_{wet} and $L_{\|}$. Shown in Fig. 2 are the divertor heat flux profiles measured in 4-5 MW NBI-heated H-modes by infrared thermography under attached divertor conditions (lower $n_e \sim (4 - 5.5) \times 10^{19}$ m^{-3}) with similar low divertor radiated power losses (1.3 MW), and the parallel heat flux profiles. The effect of A_{wet} is accounted via the angle between the total magnetic field

and the divertor target: $q_{\parallel} = q_{div}/\sin(\alpha)$, where $\alpha = 0.5 - 2°$. The inter-ELM profiles were conditionally averaged over 20-50 ms during the last 25% of the inter-ELM cycle. In all SF divertor configurations, the innermost SP (SP4 referring to Fig. 1) received low heat flux 0.1-0.3 MW/m^2, similar to the standard divertor. It is the outermost strike point(s) where the heat flow was affected via the SF geometry. Power spreading in the divertor via heat flow into additional divertor legs (SP2, SP3) was also observed in SF configurations. In the SF-minus, outer SOL power was split between SP3 and SP1. The fraction of power (and heat flux) deposited in SP3 was typically low, up to 15 % of the power measured in the SP1 at $P_{NBI} \geq 5$ MW, and undetectable at $P_{NBI} \leq 4$ MW, despite the fact that 30-60% of the SOL adjacent to the primary separatrix was connected to it. Interestingly, the SP1 received most of the heat flux, which was mitigated by A_{wet} [18]. In the nearly-exact SF, most of the outer SOL heat went into the SP1, and a small fraction (again, up to $\sim$ 10%) diffused across the null region into SP2. Heat deposition in the SF-plus was similar, except heat in the additional SPs was rarely detected. In most cases, the A_{wet} accounted for up to 80-90% of the observed divertor q_{peak} reduction, with the rest attributed to other effects, e.g. spreading to the additional SPs, and not readily quantifiable reduction due to additional diffusive spreading over the increased $L_{\parallel}$.

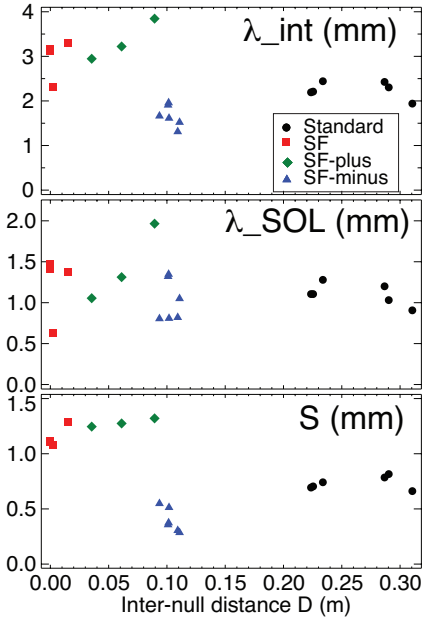

FIG. 3: Parallel heat flux profile integral width λ_{int} and its components λ_{SOL} and S for the standard and SF configurations.

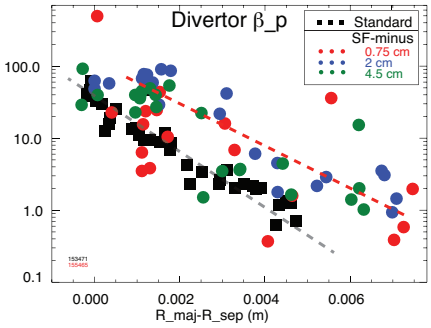

FIG. 4: Poloidal β_p measured in the divertor as a function of distance from separatrix projected to midplane. Lines are drawn to guide the eye. The SF-minus point correspond to three distances above the target as indicated.

Power sharing over multiple strike points and possible perpendicular transport modifications are viewed as attractive SF features. The effect of the increased A_{wet} on divertor heat footprint, while significant in DIII-D and NSTX, may not be readily achievable in future tokamak geometries with target plates positioned not as close to the SF null region. The spreading of heat and particle fluxes over additional divertor legs, and profile broadening in each SP, may occur due to plasma mixing in the enlarged low B_p region in the SF divertor caused by null-region ballooning, electrostatic, and flute-like MHD instabilities, as predicted theoretically [14, 19, 20]. Analysis of inter-ELM parallel heat flux profiles in the SF configurations showed the SP1 heat flux profile broadening (cf. standard divertor [17]). The measured $q(R_{div})$ is mapped to $q_{\parallel}$ as a function of radial midplane distance from separatrix. The profile is fitted with the Eich function [21], a sum of a gaussian and an exponential functions, the former characterizing symmetric radial heat spreading into the SOL and private flux region via the parameter S, and the latter characteristic of the SOL transport via the SOL power width λ_{SOL}. Shown in Fig. 3 are the integral SOL width λ_{int}, defined according to Ref. [22], and the two fitting components, λ_{SOL} and S for the outermost SP1 in the SF and standard configurations. The data points correspond to $P_{NBI} = 4.0 - 5.0$

MW H-mode discharges with lower-end densities and divertor P_{rad} matched within 15%. Larger $q\|$ widths are observed in the near-exact SF and the SF-plus, mostly as a result of the much larger S. The SOL width also appears to be affected: λ_{SOL} is larger by up to 30%. In the SF-minus, the SP1 widths are reduced, however, the interpretation is more complicated. In the SF-minus, the secondary null separates the SOL into two manifolds connected to the primary SP3 and secondary SP1. In the SP3, as discussed above, heat flow was significantly affected by the SF configuration (e.g., $L_\|$ increased by up to 70%), The second (secondary) SOL manifold with SP1, is less affected by the SF configuration. In the SP1 λ_{SOL} is similar to the standard divertor and S is smaller. Present data does not allow to separate the effect of the increased diffusive spreading due to the higher $L_\|$ and transport in the SF and SF-plus. However, the increased λ_{SOL} is an encouraging results since it may imply increased radial transport ($\lambda^2_{SOL} \sim \chi_{perp}\tau_E^{SOL}$).

In the SF configurations, the broad zone of low B_p leads to a much larger region with high poloidal beta $\beta_p = P_k/P_m = 8\pi P_k/B_p^2 \gg 1$, where $P_k = T_e n_e$ is the kinetic plasma pressure, and P_m is the poloidal magnetic plasma pressure. As conjectured theoretically, the pressure balance condition no longer holds ($\beta_p \gg 1$) and the poloidal equilibrium is not sustained. The plasma convectively mixes in the toroidally symmetric null-region manifold, and spreads toward all divertor legs. The convection may be caused by the flute-like mode driven by the toroidal field curvature and the vertical pressure gradient [20]. The size of the convective zone estimated from Ref. [20] for the DIII-D parameters is several cm. The DIII-D divertor Thomson scattering (DTS) diagnostic was used to measure plasma kinetic pressure and infer β_p in the standard and SF null regions (Fig. 4). The P_k profiles were obtained in the standard divertor configuration by slowly translating the X-point horizontally across the DTS region using the plasma control system; in the SF configuration, the translation capability was limited to a few cm. Shown in Fig. 4 is a comparison of the β_p profiles measured in the divertor X-point vicinity for the standard and SF-minus configuration. The DTS data corresponds to the inter-ELM pressure conditionally sampled in the last 50% of the ELM cycle over the translation scan, with data points taken in several spatial locations above the divertor floor (as indicated in the legend). First, divertor β_p is low in the far SOL, and rapidly approaches high values in the X-point vicinity. Second, the region of high $\beta_p \geq 10-100$ is much broader in the SF configuration. For comparison, the measured upstream SOL $\beta_{pm} \leq 0.01$. Based on the theoretical estimates [14] with DIII-D parameters, we obtain for the size of the convective zone $D^* = a(\beta_{pm})^{1/4} \sim 20$ cm for the SF, and $D^* = a(\beta_{pm})^{1/2} \sim 6$ cm for the standard divertor. During ELMs, the null-region plasma pressure significantly increases due to the ELM ion density convective pulse, and the β_p is increased by another order of magnitude. While it is not presently possible to directly measure the hypothetical mode frequency or amplitude, present divertor β_p measurements are consistent with theory [14, 19, 20] and can aid further modeling of β-dependent transport.

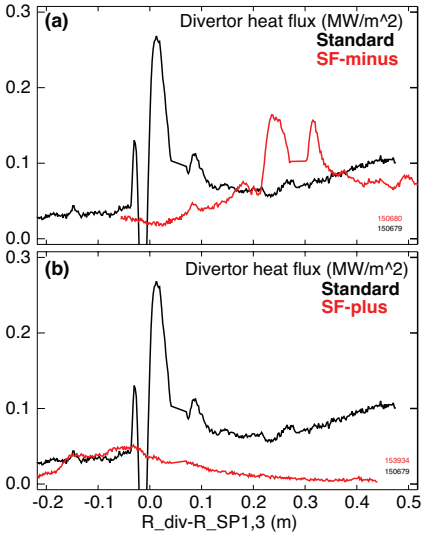

FIG. 5: Inter-ELM divertor heat flux profiles in the standard radiative, SF-minus (a), and SF-plus (b) divertors.

Additional inter-ELM divertor heat flux mitigation was achieved with dissipative losses

in the radiative SF divertor in DIII-D. In NSTX, the SF geometry facilitated detachment access due to increased volumetric power and momentum losses [11, 23]. Radiative divertor conditions in DIII-D are achieved in the standard divertor with carbon and deuterium radiation using D_2 seeding that increases upstream (and core) density [24, 25]. A comparison of the D_2-seeded radiative SF and standard divertors in DIII-D demonstrated that: 1) both the radiative SF-plus and SF-minus were compatible with the H-mode confinement albeit with confinement degradation similar to the standard divertor; 2) the onset of radiative SF conditions (e.g., increase in impurity radiation and recombination, heat flux reduction) were obtained at core n_e similar (within 10-20%) to the standard radiative divertor; 3) the reduction of inter-ELM divertor heat fluxes was stronger in the SF-plus and SF-minus configurations; 4) radiated power was more broadly distributed in the SF configurations, including the additional divertor legs; 5) In the SF-plus, a higher degree of power sharing among SPs was observed at higher divertor n_e.

While the confinement degradation was not associated with the SF formation at lower-to-medium densities, additional D_2 seeding at rates 50–80 Torr l/s (to raise the density for radiative divertor onset) resulted in 10%-20% reduction in, e.g., H98(y,2) and H89L factors and plasma stored energy W_{MHD} in the standard divertor, and up to 30% in H-mode discharges with the radiative (higher-density) SF-plus or SF-minus. The degradation was associated with the reduction of pedestal T_e^{ped} and hence pedestal energy [18]. Further H-mode scenario development is necessary to optimize compatibility of the core plasma with radiative SF, as is typically done with the standard radiative divertor (e.g., Ref. [26]).

A greater reduction factor of inter-ELM peak divertor heat flux was measured in the radiative SF divertor than in the standard radiative divertor at $P_{NBI} = 4 - 5$ MW. The profiles are compared in Fig. 5. In the standard divertor, the partial detachment led to a significant (up to x10) peak heat flux reduction (cf. Fig. 2). In the radiative SF-minus and SF-plus, a nearly complete power detachment was observed, as heat flux in SP1 was barely detectable. The A_{wet} factor accounted for most of the difference between the radiative SF-minus and the standard divertor, while in the SF-plus case, the difference was greater. Experiments at high P_{SOL} are needed to study possible differences in detachment characteristics between the SF and the standard divertor, e.g., the effect of neutrals, transport and radiation limits.

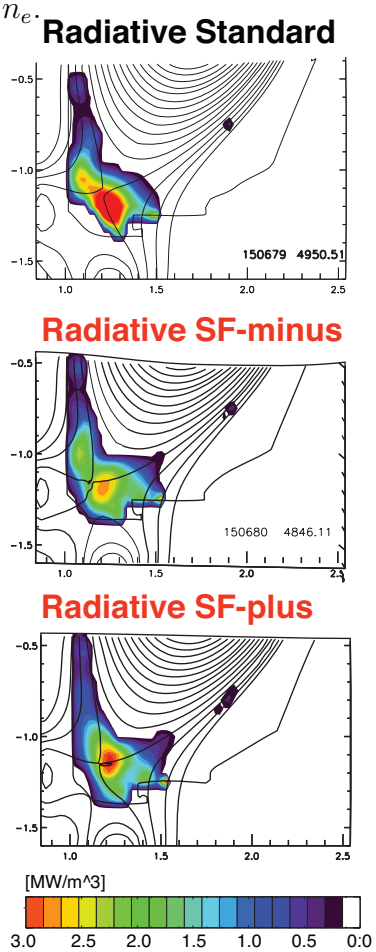

FIG. 6: Radiated power density distribution in the radiative standard (a) and SF-minus (b), and SF-plus (c) configurations.

Divertor radiated power from carbon and deuterium species was distributed more broadly and uniformly in the radiative SF configurations. Spreading the radiation could be an additional benefit as it reduces gradients and the peak radiative heating of divertor targets. Shown in Fig. 6 are radiated power distributions in the radiative standard and SF divertors, obtained from tomographic reconstructions of multi-channel bolometry data. The lower divertor radiated power was about 2 MW in the radiative standard, SF-plus or minus configurations, differing by 10%-15% (cf. $P_{SOL} \sim 3.0 - 3.5$ MW). In the standard

divertor, radiation initially peaked in the inner and outer divertor legs, and at the partial detachment onset, the radiative front moved to the X-point (e.g., Ref. [25]). In the SF-minus, radiation also initially peaked in the divertor legs, and, as the SF-minus was formed, it broadly distributed throughout the divertor volume, with occasional peaking at the null-points. In the SF-plus, the radiation front was formed in the divertor legs and moved toward the null-point region where it stabilized. The extended connection length region enabled a broader radiation zone. Also, despite the geometric effects (e.g., increase in $L_{||}$ by 50%-75%), the SF configurations were not more likely than the standard divertor to form X-point radiative instabilities that can degrade the confinement.

The broader low B_p zone extended into the edge of the confined plasma and weakly modified its magnetic properties. In the pedestal region, both the magnetic shear and q_{95} were systematically increased by 10%-30%. The pedestal stored energy lost per ELM ΔW_{ELM} was reduced as higher q_{95} increased the pedestal collisionality $\nu^*_{ped} = \pi R q_{95}/\lambda_{e,e}$ and the ELM parallel transit time $\tau^{ELM}_{||} = 2\pi R q_{95}/c_{s,ped}$ (the pedestal ion transport time from the mid plane to the target at the sound speed c_s). This was consistent with the Type I ELM scaling of ΔW_{ELM} with ν^*_{ped} found in many tokamaks [27]. In some discharges, the effect was strong, ΔW_{ELM} was reduced by up to 50% [13]. More typically, however, the reduction was in the range 5%-20%. At higher density in radiative SF divertor discharges, both the ΔW_{ELM} and $\Delta W_{ELM}/W_{ped}$ were lower by 10%-20% (cf. standard divertor) [18]. Kinetic profiles were similar with and without the SF configurations. Pedestal top plasma parameters were modestly changed within $\sim$ 15%: with the SF, T^{ped}_e slightly reduced, n^{ped}_e slightly increased, and p^{ped}_e remained nearly constant. Pedestal energy W_{ped} was nearly unaffected at lower n_e. However, some additional degradation of the pedestal T_e was noted in highly radiative SF configurations, leading to the pedestal energy reduction. Changes in the magnetic shear and weak changes in pedestal pressure gradient did not apparently affect the stability of the peeling-balooning modes, as only small changes in ELM frequency (about 10%-20%) were detected with the SF.

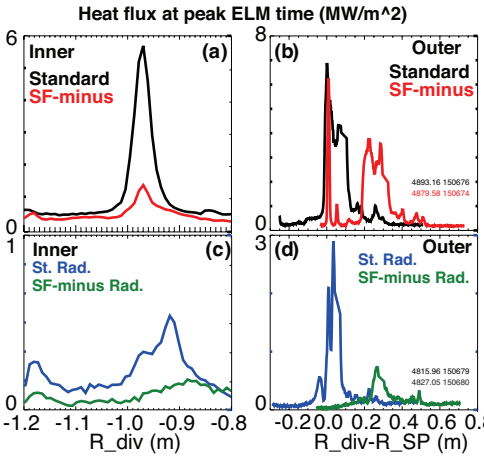

FIG. 7: Divertor heat flux profiles at peak ELM times in the SF-minus configuration.

The SF configuration led to the reduction of ELM energy and ELM divertor heat fluxes both at lower n_e and higher n_e (at radiative conditions). The increased $L_{||}$ leads to reduced target surface temperature rise as $\Delta T_t \sim \Delta W_{ELM}/\sqrt{\tau_d}$, where τ_d is the ELM deposition time which is increased at longer $L_{||}$ [28]. The fast convective transport in the low B_p region driven by instabilities [14] can lead to the ELM heat flux sharing among the additional strike points. In radiative SF divertor experiments in DIII-D both the ΔW_{ELM} and the divertor q^{ELM}_{peak} were reduced more strongly than in standard radiative divertor, leading to the much reduced peak powers. Shown in Fig. 7 are representative divertor heat flux profiles at peak ELM time in discharges with the SF-minus and standard divertors. At lower n_e, heat flows to all strike points in the SF divertor and q^{ELM}_{peak} is reduced, and nearly eliminated in the radiative SF, both in the inner strike point and the outer strike points. The peak divertor power was reduced in the SF-minus by up to 50-70%, and further

reduced in the radiative SF-minus by up to 50%, as compared to the standard divertor [18], suggesting that enhanced radiative dissipation, geometric effects and power spreading all played a role. The analysis of ELM plasma-wetted areas $A_{wet}^{ELM} = P_{div}^{ELM}/q_{peak}^{ELM}$, where P_{div}^{ELM} is the divertor power received during an ELM, showed no systematic trends in the outer divertor, and a reduced A_{wet}^{ELM} in the inner divertor in the SF configuration, both at lower n_e and at higher n_e (radiative) conditions. A similar significant reduction of ELM heat fluxes was also observed in the radiative SF divertor in NSTX [12].

In summary, the emerging understanding of inter-ELM and ELM divertor heat transport in the radiative SF divertor from recent DIII-D experiments provides support to the snowflake divertor concept as a promising solution for divertor heat flux mitigation in future magnetic fusion devices. The experiments demonstrated the SF divertor compatibility with high H-mode confinement, radiative divertor with gas seeding, and led to reduced ELM energies, as well as divertor heat fluxes between and during ELMs. Radial broadening of the parallel heat flux profiles suggest increased radial transport in the SOL.

Acknowledgments This work was performed under the auspices of the U.S. Department of Energy under Contracts DE-AC52-07NA27344,* DE-AC02-09CH11466 and DE-FC02-04ER54698. We thank the entire DIII-D Team for technical, engineering and computer support as well as plasma and diagnostic operations.

References

[1] ITER Physics Expert Group on Divertor et al., Nucl. Fusion **39** (1999) 2391.
[2] LOARTE, A. et al., Nucl. Fusion **47** (2007) S203.
[3] PENG, Y.-K. et al., Plasma Phys. Control. Fusion **47** (2005) 263.
[4] CHAN, V. et al., Nucl. Fusion **51** (2011) 083019.
[5] ZOHM, H., Fus. Eng. Design **88** (2013) 428.
[6] RYUTOV, D., Phys. Plasmas **14** (2007) 064502.
[7] PIRAS, F. et al., Phys. Rev. Lett. **105** (2010) 155003.
[8] REIMERDES, H. et al., Plasma Phys. Control. Fusion **55** (2013).
[9] VIJVERS, W. et al., Nucl. Fusion **54** (2014) 023009.
[10] SOUKHANOVSKII, V. et al., Nucl. Fusion **51** (2011) 012001.
[11] SOUKHANOVSKII, V. et al., Phys. Plasmas **19** (2012) 082504.
[12] SOUKHANOVSKII, V. et al., J. Nucl. Mater. **438** (2013) S96.
[13] HILL, D., Nucl. Fusion **53** (2013) 104001.
[14] RYUTOV, D. et al., Plasma Phys. Control. Fusion **54** (2012).
[15] GREENWALD, M. et al., Nucl. Fusion **28** (1988) 2199.
[16] KOLEMEN, E. et al., This conference, Paper PPC/1-1 (2014).
[17] MAKOWSKI, M. A. et al., Phys. Plasmas **19** (2012) 056122.
[18] SOUKHANOVSKII, V. A. et al., Submitted to J. Nucl. Mater. (2014).
[19] RYUTOV, D. et al., in *Proc. 24th IAEA FEC, San Diego, 2012*, Paper TH/P4-18.
[20] RYUTOV, D. et al., Phys. Scripta **89** (2014) 088002.
[21] EICH, T. et al., Phys. Rev. Lett. **107** (2011) 215001.
[22] LOARTE, A. et al., J. Nucl. Mater. **266–269** (1999) 587.
[23] MEIER, E. T. et al., Submitted to J. Nucl. Mater. (2014).
[24] PETRIE, T. et al., Nucl. Fusion **37** (1997) 321.
[25] FENSTERMACHER, M. E. et al., Plasma Phys. Control. Fusion **41** (1999) A345.
[26] PETRIE, T. et al., J. Nucl. Mater. **363–365** (2007) 416.
[27] LOARTE, A. et al., J. Nucl. Mater. **313–316** (2003) 962.
[28] ROGNLIEN, T. et al., J. Nucl. Mater. **438** (2013) S418.

*LLNL